Published in final edited form as:
Mol Imaging. 2011 June ; 10(3): 153–167.

Early Therapy Evaluation of Combined Cetuximab and Irinotecan in Orthotopic Pancreatic Tumor Xenografts by Dynamic Contrast-Enhanced Magnetic Resonance Imaging

Hyunki Kim, **Karri D. Folks**, **Lingling Guo**, **Jeffery C. Sellers**, **Naomi S. Fineberg**, **Cecil R. Stockard**, **William E. Grizzle**, **Donald J. Buchsbaum**, **Desiree E. Morgan**, **James F. George**, and **Kurt R. Zinn**
Departments of Radiology, Biomedical Engineering, Surgery, Biostatistics, Pathology, Radiation Oncology, and Medicine and Comprehensive Cancer Center, University of Alabama at Birmingham, Birmingham, AL.

Abstract

Early pancreatic cancer response following cetuximab and/or irinotecan therapies was measured by serial dynamic contrast-enhanced magnetic resonance imaging (DCE-MRI) before and during therapy. Groups 1 to 4 (n = 6/group) of SCID mice bearing orthotopic pancreatic adenocarcinoma xenografts expressing luciferase were treated with phosphate-buffered saline, cetuximab, irinotecan, or cetuximab combined with irinotecan, respectively, twice weekly for 3 weeks. DCE-MRI was performed on days 0, 1, 2, and 3 after therapy initiation, whereas anatomic magnetic resonance imaging was performed on days 0, 1, 2, 3, 6, and 13. Bioluminescence imaging was performed on days 0 and 21. At day 21, all tumors were collected for further histologic analyses (Ki-67 and CD31 staining), whereas tumor dimensions were measured by calipers. The K^{trans} values in the 0.5 mm–thick peripheral tumor region were calculated, and the changes in K^{trans} during the 3 days posttherapy were compared to tumor volume changes, bioluminescent signal changes, and histologic findings. The K^{trans} changes in the peripheral tumor region after 3 days of therapy were linearly correlated with 21-day decreases in tumor volume ($p < .001$), bioluminescent signal ($p = .050$), microvessel densities ($p = .002$), and proliferating cell densities ($p = .001$). This study supports the clinical use of DCE-MRI for pancreatic cancer patients for early assessment of an anti–epidermal growth factor receptor therapy combined with chemotherapy.

Pancreatic cancer has the highest fatality rate of all cancers and is the fourth leading cause of cancer death in the United States.[1] The nonspecific and variable symptoms of pancreatic cancer often lead to late-stage disease at the time of diagnosis, and the majority of the newly diagnosed pancreatic cancers are unresectable.[2] Gemcitabine is a standard drug for unresectable pancreatic cancer[3]; a small survival benefit of radiation therapy in combination with gemcitabine has been reported in patients with localized unresectable pancreatic cancer compared to gemcitabine monotherapy,[4] whereas any of the conventional chemotherapeutic agents, such as 5-fluorouracil, cisplatin, irinotecan, and oxaliplatin, did not improve the survival of patients with advanced pancreatic cancer when added to gemcitabine.[5–8]

Address reprint requests to: Hyunki Kim, PhD, VH G082C5, University of Alabama at Birmingham, Birmingham, AL 35294-0012; Hyunki@uab.edu.

Financial disclosure of reviewers: None reported.

More recently, anti–epidermal growth factor receptor (EGFR) has been investigated as a targeted therapy for pancreatic cancer. EGFR regulates cell proliferation and differentiation and is expressed in a marked percentage of cases ranging from 45 to 95%.[9,10] EGFR expression is associated with aggressive tumor growth and poor clinical prognosis.[11] Erlotinib (a small molecule targeting EGFR) or cetuximab (anti-EGFR monoclonal antibody) combined with gemcitabine significantly improved the survival of patients with advanced pancreatic cancer over gemcitabine monotherapy.[10,12] Combination therapy with erlotinib and gemcitabine is considered a newer standard for locally advanced, unresectable, or metastatic pancreatic cancer, recently approved by the Food and Drug Administration.

However, there is a wide range of drug sensitivities among individuals with pancreatic cancer. Because the characteristics of an individual tumor vary among patients, it would be ideal to tailor the therapeutic strategy to each patient by detecting the early tumor response and in turn to increase the probability for a favorable outcome. Individualized optimal treatment, called personalized medicine, can be guided by molecular biomarkers obtained from biopsies or by the use of imaging biomarkers. Although minimally invasive biopsy techniques are available,[13] they still involve pain, stress, and risk to patients. Biopsies can potentially stimulate neoangio-genesis by damaging tumor tissue and can also increase the risk of metastases by increasing circulating tumor cells. It has also been argued that data obtained from a small portion of the tumor mass may not be representative of the entire tumor response. This may be particularly important when the response to therapy is tumor necrosis. Therefore, noninvasive imaging might be an approach that addresses these problems for pancreatic cancer patients as it can minimize patient discomfort and the risk of inducing metastasis and can be used to evaluate the response of the entire tumor to therapy.

Dynamic contrast-enhanced magnetic resonance imaging (DCE-MRI) noninvasively measures pharmacokinetic parameters in microvasculature by quantifying the transfer of a contrast agent from the vascular space to the extravascular-extracellular space over time.[14] Effective cancer therapies disrupt tumor vascular angiogenesis, leading to a decrease in microvessel density, perfusion, and permeability. These features can be measured by DCE-MRI prior to a quantifiable tumor volume decrease or morphologic change. DCE-MRI has been clinically used for evaluating the early therapeutic efficacy of drugs for solid cancers such as glioblastoma,[15] breast cancer,[16,17] head and neck cancer,[18] colorectal cancer,[19] and renal cell cancer.[20]

The purpose of this study was to evaluate DCE-MRI as an early prognostic tool to identify and characterize effective anti-EGFR therapy with and without concurrent chemotherapy using cetuximab and irinotecan in an orthotopic murine pancreatic cancer model.

Materials and Methods

Reagents and Cell Lines

All reagents were from Fisher Scientific (Pittsburgh, PA) unless otherwise specified. The human pancreatic cell line, MIA PaCa-2, was a gift from Dr. M. Hollingsworth (University of Nebraska). MIA PaCa-2 cells were cultured in Dulbecco's Modified Eagle's Medium (DMEM) (Mediatech Inc, Herndon VA) supplemented with 10% fetal bovine serum (Hyclone, Logan, UT). Luciferase-positive Mia PaCa-2 cells were created using the ViraPort retroviral vector, which does not require antibiotics for selection (Stratagene, La Jolla, CA). After viral infection according to the manufacturer's instructions, Mia PaCa-2 cells were cloned by limiting dilution to produce a stable luciferase-positive cell line. Single colonies were screened based on luminescence signal obtained with the IVIS-100 system (Xenogen, Inc., Alameda, CA). The luciferase-positive Mia PaCa-2 clone was propagated and used for the mice of groups 1 to 6, whereas the parent Mia PaCa-2 cells were used for

the mice of groups 7 and 8. Luciferin was purchased from Xenogen, Inc. Cetuximab (ImClone Systems Incorporated, Branchburg, NJ), irinotecan (Pfizer, Inc., New York, NY), and Prohance (gadoteridol, a magnetic resonance contrast agent; Bracco Diagnostics Inc., Princeton, NJ) were purchased from the University of Alabama at Birmingham (UAB) Hospital Pharmacy. Purified mouse IgG1 κ isotype control antibody was purchased from SouthernBiotech (Birmingham, AL). Fresh technetium 99m pertechnetate was purchased from Birmingham Nuclear Pharmacy (Birmingham, AL).

Animal Preparation

Animal experiments were reviewed and approved by the Institutional Animal Care and Use Committee. Eight groups of female SCID BALB/c mice (NCI-Frederick Animal Production Program, Fredrick, MD; 4–5 weeks old, $n = 6$ for groups 1–4, $n = 3$ for group 5, $n = 4$ for groups 6 and 7, $n = 5$ for group 8) were used. The procedure for intrapancreatic tumor implantation was the following: a 1 cm incision was made in the left upper quadrant of the abdomen of anesthetized mice, and a solution of 2.5×10^6 MIA PaCa-2 cells in 40 μL of DMEM was injected into the tail of the pancreas. The skin and peritoneum were closed in one layer with three interrupted 5-0 Prolene sutures. At 24 days after tumor cell implantation, abdominal ultrasound imaging was performed as described below to select mice with matched tumor size for groups 1 to 6. At 28 days after tumor cell implantation, a vascular access port (PennyPort, Access Technologies, Skokie, IL) was subcutaneously implanted on the right chest of each mouse in groups 1 to 6 and the catheter connected to the port was inserted into a jugular vein to facilitate repeated intravenous gadoteridol injections. The detailed procedure of port implantation and maintenance is provided in the Appendix. Imaging and therapy were initiated at 4 days after port insertion (32 days after tumor cell implantation). Table 1 shows the animal groups, injected doses, imaging modalities, and imaging times for groups 1 to 8. Groups 1 to 4 were intraperitoneally injected with phosphate-buffered saline (PBS; serving as control), cetuximab (1 mg), irinotecan (25 mg/kg body weight), and cetuximab combined with irinotecan, respectively, on days 0, 3, 7, 10, 14, and 17. Groups 5 and 6 were intraperitoneally injected with PBS and cetuximab (1 mg) combined with irinotecan (25 mg/kg body weight), respectively, on days 0 and 3; this was a repeated experiment to confirm the data obtained from groups 1 to 4. Two animals of group 2 died at 9 and 19 days after therapy initiation, whereas three animals of group 3 died at 7, 9, and 12 days after therapy initiation. All imaging was performed before drug dosing on each day. DCE-MRI was performed on days 0, 1, 2, and 3 for groups 1 to 4 and on days 0 and 3 for groups 5 and 6. Anatomic MRI was performed on days 0, 1, 2, 3, 6, and 13 for groups 1 to 4 and on days 0, 3, and 6 for groups 5 and 6. Bioluminescence imaging was performed on days 0 and 21 for groups 1 to 4 and on days 0, 3, and 6 for groups 5 and 6; planar bioluminescence imaging may induce severe quantification error for orthotopic pancreatic tumors owing to optical light attenuation,[21] so it was applied only at two imaging time points, before and after the entire study for groups 1 to 4, just to confirm the therapeutic efficacy measured by tumor volume regression. At day 21, all tumors of groups 1 to 4 were collected by dissection for further histologic analyses (Ki-67 and CD31 staining), whereas tumor volume was calculated using the following equation:

$$Volume = xyz(\pi/6)$$

where x, y, and z are three orthogonal dimensions of a tumor measured with a caliper (Hexagon Metrology, Inc., North Kingstown, RI). To assess distribution of cetuximab, animal groups 7 and 8 were intravenously injected with ^{99m}Tc-labeled isotype control antibody (3.0 ± 0.7 MBq, 5.9 ± 1.4 μg) and ^{99m}Tc-labeled cetuximab (4.6 ± 0.3 MBq, 8.7 ± 0.5 μg), respectively, and single-photon emission computed tomography (SPECT) and x-ray

computed tomography (CT) were applied at 6 hours after injection, followed by a biodistribution study at 24 hours after injection. The mean tumor weights of groups 7 and 8 were not statistically different ($p = .843$). All animals were anesthetized using isoflurane gas (1–2%) during imaging.

SPECT/CT Imaging and Biodistribution Study

SPECT/CT imaging and biodistribution study were performed to measure the tumor uptake of ^{99m}Tc-labeled cetuximab in vivo. A fresh 1.8 mM solution of succinimidyl 6-hydrazinonicotinate (HYNIC, courtesy of Dr. Gary Bridger, AnorMED, Inc., Langley, BC) in dimethylformamide was prepared. A solution containing 40 pmol was transferred to glass vials, followed by freezing at −90°C; then the solutions were lyophilized using an Advantage Benchtop Freeze Dryer (Virtis Co Inc., Gardiner, NY) with the shelf temperature at −75°C and trap at −90°C. The vials were sealed under vacuum and kept frozen at −80°C until use. Each vial was reconstituted with 1.0 mL of sodium phosphate buffer (0.15 M, pH 7.8) containing 1 mg of cetuximab or isotype control antibody (HYNIC to antibody molar ratio = 6).[22] After a 3-hour incubation at room temperature, the mixture was dialyzed using membrane with a 10,000 kDa molecular weight cutoff (Pierce, Rockford, IL) in PBS (pH 7.4) overnight at 4°C. The HYNIC-modified cetuximab or isotype control antibody was labeled with ^{99m}Tc using $SnCl_2$/tricine as the transfer ligand,[23] and unbound ^{99m}Tc was removed by G-25 Sephadex size exclusion chromatography. The radiolabeling yield was approximately 60%. Protein concentrations of the collected fractions were measured by the Lowry assay.[24] The level of ^{99m}Tc binding to antibody was greater than 97%, as measured by thin-layer chromatography using separate strips eluted with saturated saline and methyl ethyl ketone.

SPECT/CT imaging was performed using a SPECT/CT dual-modality imager (X-SPECT, Gamma Medica-Ideas, Northridge, CA). In SPECT imaging, 64 projections (data matrix size: 56 × 56 per projection) were acquired with a 50-second acquisition time per projection, using a pinhole collimator with a 1 mm tungsten pinhole insert. The field of view was 47.9 mm, whereas the radius of rotation was 35 mm. Images were reconstructed using an ordered subsets expectation maximization algorithm (8 subsets and 20 iterations). The fourth-order Butterworth digital filtrations (fc = 0.25, fm = 0.15) provided by the vendor software were applied for all SPECT images to enhance the image quality. For the CT system, the x-ray tube was operated at a voltage of 50 kV_p and an anode current of 0.6 mA. To obtain the CT images, 256 projections were acquired, and acquisition time per projection was 0.5 seconds. The coregistration of SPECT and CT images was performed using computer software, *IDL Virtual Machine* (Research System Inc, Boulder, CO). A 60 W heat lamp warmed the animal bodies while they were under anesthesia. A consistent color scale was applied to all SPECT images after correction for radioactive decay and dose.

Tumor and blood were collected for each animal of groups 7 and 8. Those samples were weighed and the ^{99m}Tc activity was measured using a calibrated gamma ray counter (MINAXIγ Auto-gamma 5000 series Gamma Counter manufactured by Packard Instrument Company, Grove, IL), decay corrected to dosing time, and converted to absolute radioactivity, and then the percentage of injected dose per gram of each tissue (% ID/g) together with tumor to blood ratio was determined.

Magnetic Resonance Imaging

DCE-MRI was used to assess the change in intratumoral vascularity following anti-EGFR therapy and/or chemotherapy, whereas anatomic MRI was used to monitor tumor volume change during therapy. Small-animal MRI was performed on a Bruker BioSpec 9.4 T system (Bruker BioSpin Corp., Billerica, MA). The animal was placed in an animal bed equipped

with circulating warm water to regulate body temperature during MRI. An orthogonally bent plastic board was used to prevent the transfer of the respiratory motion in the chest to abdominal area.[21] The tumor was imaged using a combination of a ^{1}H volume resonator/transmitter and a surface coil receiver (Bruker BioSpin Corp.). The respiratory rate of animals was monitored using an MRI-compatible small-animal respiratory monitoring device (SA Instrument, Inc., Stony Brook, NY) during imaging. A 27-gauge needle connected to a sterilized polyurethane tube (outer diameter × inner diameter: 0.84 mm × 0.34 mm; Strategic Applications Inc., Libertyville, IL) was inserted perpendicularly into the lumen of each port to deliver gadoteridol. Anatomic MRI to measure tumor volume was performed using a T_2-weighted spin-echo sequence (RARE) with the following acquisition parameters: repetition time (TR)/echo time (TE) = 2,000/34 milliseconds, 128 × 128 matrix, and a 30 × 30 mm field of view. One millimeter–thick slices with a 0.2 mm gap were used to cover the entire tumor region. Then a T_1 map was acquired with a gradient-echo multiflip-angle approach with the following parameters: TR/TE = 115/3 milliseconds, 128 × 128 matrix, a 30 × 30 mm field of view, number of excitation = 4, and seven flip angles of 10, 20, 30, 40, 50, 60, and 70°. A maximum of five 1 mm–thick slices (0.2 mm gap) were used to cover the tumor region of interest (ROI). DCE-MRI employed the same acquisition parameters as those above but with the fixed flip angle of 30°. Five baseline images were acquired before gadoteridol injection, and then 20 images were acquired after gadoteridol injection of 0.0267 mmol/mL over a period of 15 seconds with a total injection volume of 0.15 mL; the mean animal body weight of groups 1 to 6 was 18.1 ± 0.3 g (n = 31) when excluding port weight (1.6 g) on day 0, so the mean weight-based dose was 0.223 ± 0.004 mmol/kg on that day. A syringe pump (NE-1600, New Era Pump Systems, Inc., Wantagh, NY) was used to inject gadoteridol at a constant rate (0.01 mL/s).

The reference region (RR) model was employed to calculate volume transfer constant (K^{trans}) and fractional extravascular-extracellular volume (ν_e).[25] The RR model is based on the flow-limited Kety model[26] and uses the signal enhancement in an RR to remove the need for the arterial input function (AIF) as follows;

$$C_{t,ROI}(t)=(K^{trans,ROI}/K^{trans,RR})C_{t,RR}(t)+(K^{trans,ROI}/\nu_{e,RR})\int_0^t C_{t,RR}(t')dt'-(K^{trans,ROI}/\nu_{e,ROI})\int_0^t C_{t,ROI}(t')dt' \quad (1)$$

where $C_{t,ROI}(t)$, $K^{trans,ROI}$, and $\nu_{e,ROI}$ are the contrast agent concentration, volume transfer constant, and fractional extravascular-extracellular volume, respectively, in the tumor, whereas $C_{t,RR}(t)$, $K^{trans,RR}$, and $\nu_{e,RR}$ are those in the RR. Thirty-two voxels (two 4 × 4 voxel windows) located in the perivertebral muscle were selected as the RR, and the $\nu_{e,RR}$ was assumed to be constant at 0.08 over the region.[27] The fifth-order polynomial curve fitting into each contrast agent concentration curve was used to suppress a sudden signal variation owing to noise or animal motion. The tumor area was segmented from the anatomic MRIs using the signal intensity difference between the ROI and background, whereas the intensity thresholds were determined manually. In addition, the isodistance peripheral region with 0.5 mm thickness beginning from the tumor surface was segmented for each slice, whereas the random topologic structure of the tumor was maintained. After the tumor boundary was detected, the distances from each voxel inside the boundary to all voxels located on the boundary were calculated. The voxels whose minimum distances were less than 0.5 mm were segmented. The K^{trans} and ν_e values of each voxel were obtained using equation (1) and averaged in either the whole tumor region or the peripheral tumor region. The negative K^{trans} and ν_e values were replaced with 0, and the ν_e values larger than 1 were replaced with 1. Tumor volume was calculated by summing all voxels inside the tumor boundary of the anatomic MRIs. Segmentation of the whole tumor area was performed using *ImageJ* version 1.40 (National Institutes of Health, Bethesda, MD). The

K^{trans} and v_e quantification, peripheral tumor region segmentation and tumor volume calculation were implemented using computer software developed using *Labview* version 8.5 (National Instruments Co., Austin, TX). The best-fitting quadratic polynomial curves for K^{trans} change in the peripheral tumor regions over 3 days following therapy were obtained for groups 1 to 4, and the quadratic coefficient was proposed as a novel DCE-MRI-based biomarker to enable early prognostic decisions independent of imaging time. Linear and quadratic polynomial regressions were performed using *Excel* version 11.3.6 (Microsoft Corporation, Seattle, WA).

Ultrasound Imaging

Ultrasound imaging was employed to select mice with matched tumor size. Ultrasound imaging was performed using a VisualSonics VEVO 660 high-frequency, high-resolution ultrasound instrument with a 40 MHz probe (Toronto, ON). Animals were placed in the supine position for examination with B-mode imaging.[28] The largest diameter was found in the anterior-posterior plane, and this diameter and a transverse diameter were measured to quantify tumor area (length × width). Mice with nonspherical tumors as determined by ultrasonography were excluded from further study.

Bioluminescence Imaging

Bioluminescence imaging was used to achieve additional therapeutic indicator complementary to magnetic resonance biomarkers. Bioluminescence imaging was performed for all mice after MRI on each day using the IVIS-100 imaging system (Xenogen, Inc., Alameda, CA). Each mouse from groups 1 to 6 was intraperitoneally injected with luciferin at a dose of 2.5 mg (0.1 mL) and imaged after 15 minutes on a temperature-controlled warm bed (37°C) with the following imaging parameters: 5 to 10 seconds of luminescent exposure time, 8 photographic binning, 25 cm axial field of view, and 1 f-stop. The ROI was drawn manually around the tumor area, and the light emitted from the ROI was measured using the vendor software.

Histologic Analyses

CD31 and Ki-67 staining were performed to analyze microvessel density and proliferating cell density, respectively. CD31 and Ki-67 staining were analyzed in each tumor of groups 1 to 4. The detailed tumor tissue staining procedure is presented in the Appendix. Two digital pictures (×400) were taken away from areas of necrosis but otherwise randomly for each tumor slice, using a SPOT camera on a Nikon Optiphot-2 microscope (Nikon Inc., Melville, NY), interfaced with a personal computer and SPOT software. The image analysis software was *ImageJ* version 1.37v. The proliferating, Ki-67-positive cancer cells were segmented by the signal intensity difference between the target cells and background in each picture, whereas the intensity and minimum particle-size thresholds were determined manually and then counted in the two pictures per tumor. The number of total cancer cells was also counted with the same procedure, and the cell density (proliferating cancer cell number/total cancer cell number) was calculated. Uneven background intensity was corrected using the "Rolling Ball" algorithm,[29] whereas the radius was manually determined. The CD31-stained area was segmented in the same way, and the area fraction (CD31-stained area/total area), considered microvessel density, was calculated.

Statistical Analysis

SPSS version 16.0 (SPSS Inc, Chicago, IL) was used to analyze the data, and p values ≤ .05 were considered significant. K^{trans}, v_e, and tumor volume measurements made among groups 1 to 4 over 3 days (or at 21 days for tumor volume) were analyzed using two-way repeated measures analysis of variance (ANOVA).[30] Treatment groups were considered a

grouping factor and measurements made on days 0 to 3 were the repeated measure. Comparisons for a single measurement were done using one-way ANOVA[31] followed by the Tukey honestly significant differences test.[32] The Pearson correlation coefficient was used to analyze the relationships between two variables.[33] Data are presented as means ± SE (standard error).

Results

SPECT/CT and biodistribution analyses confirmed specific retention of ^{99m}Tc-labeled cetuximab in orthotopic pancreatic tumor xenografts. Figure 1A presents in vivo SPECT/CT fused images (transaxial view) showing distribution of ^{99m}Tc-cetuximab (upper row) or ^{99m}Tc-isotype control antibody (lower row) of two representative mice bearing orthotopic pancreatic tumors at 6 hours after intravenous dose injection. The tumor boundary is indicated with a white dotted circle in each subfigure of Figure 1A. Figure 1B shows the biodistribution of ^{99m}Tc-labeled cetuximab or isotype control antibody in blood and tumor, together with tumor to blood ratio at 24 hours postdosing. Tumor retention of ^{99m}Tc-cetuximab was about threefold higher than that of ^{99m}Tc-isotype control antibody with statistical significance ($p < .001$), whereas the blood retentions of the two agents were not different ($p = .949$).

DCE-MRIs of orthotopic pancreatic tumor xenografts were successfully obtained with minimal motion artifact. Figure 2, A and B, shows representative DCE-MRIs at 1 minute before (see Figure 2A) and 2 minutes after (see Figure 2B) gadoteridol injection with the same intensity scale, whereas the tumor boundary is indicated with the white dotted circle in Figure 2A. Figure 2, C to F, presents the K^{trans} (see Figure 2, C and D) or ν_e (see Figure 2, E and F) maps of the tumor with the same intensity scale in the entire tumor region (see Figure 2, C and E) or 0.5 mm–thick peripheral tumor region (see Figure 2, D and F). Figure 2G shows the contrast enhancement curves averaged in the RR and the ROI indicated with the white square (4 × 4 window: 16 pixels, located in the perivertebral muscle) and the black rectangle (2 × 1 window: 2 pixels, located in the tumor), respectively, in Figure 2B, together with the best-fitting fifth-order polynomial curves.

The K^{trans} increase in the peripheral tumor region was significantly suppressed by irinotecan or combined therapy after 3 days. Figure 3 shows the K^{trans} (see Figure 3, A and B) or ν_e (see Figure 3, C and D) changes in groups 1 to 4 during 3 days posttherapy in the entire tumor region (see Figure 3, A and C) or peripheral tumor region (see Figure 3, B and D). The initial K^{trans} values of the four groups at day 0 were 0.032 ± 0.002 min^{-1} and 0.050 ± 0.003 min^{-1} in the entire and peripheral tumor regions, respectively, without statistical difference among groups in either region ($p > .05$). When analyzed in the entire tumor region, no statistical difference was detected in the K^{trans} changes between any of the groups (see Figure 3A), but in the peripheral tumor region, the significant suppression of K^{trans} increase was detected after irinotecan ($p = .008$) or combination therapy ($p < .001$) (see Figure 3B). The standard errors of K^{trans} changes on each time point relative to day 0 were 48 ± 6% lower in the peripheral tumor region compared to those in the entire tumor region ($n = 12$; $n = 3$ per group). In the repeated experiment (groups 5 and 6), the K^{trans} changes for 3 days after combined therapy (group 6) were −16 ± 12% and −19 ± 8% in the entire and peripheral tumor regions, respectively, whereas those of the control (group 5) were 105 ± 110% and 141 ± 60% in the same regions, respectively; the difference between groups 5 and 6 was significant in the peripheral tumor region ($p = .0260$) but not in the entire tumor region ($p = .2533$). The initial ν_e values of groups 1 to 4 at day 0 were 0.31 ± 0.02 and 0.39 ± 0.03 in the entire and peripheral tumor regions, respectively, without statistical difference among groups in either region ($p > .05$). The ν_e changes for 3 days in groups 1 to 4 were not different statistically in either the entire or the peripheral tumor region ($p > .05$) (see Figure

3, C and D), although the standard errors of v_e changes on each time point relative to day 0 decreased 7 ± 9% by the peripheral region analysis, consistent with the results of the repeated experiment using groups 5 and 6 (data not shown).

Early K^{trans} change was significantly correlated with long-term tumor volume and bioluminescent signal changes. Figure 4A shows tumor volume changes during 21 days of therapy. The initial tumor volume of the four groups at day 0 averaged 103 ± 9 mm^3 without statistical difference among groups ($p > .050$). The mean tumor volumes of all four groups increased about 20% during the first 3 days without statistical difference ($p > .050$), but for the entire 3 weeks of therapy, the tumor volume was significantly less for either monotherapy or combined therapy ($p < .050$) compared to control. Given that the tumor volumes at day 3 were not statistically different among the groups, those at days 1 and 2 were not further analyzed. The mean tumor volume changes for group 5 were 26 ± 7% and 45 ± 3% at 3 and 6 days after therapy initiation, respectively, whereas those of group 6 were 12 ± 4% and 5 ± 7%, respectively, on the same days. The tumor volume difference between groups 5 and 6 was statistically significant on day 6 ($p = .0045$) but not on day 3 ($p = .1284$). Figure 4B shows bioluminescent signal changes of groups 1 to 4 during 21 days after therapy initiation, normalized to the mean value of group 1. The initial bioluminescent signals of groups 1 to 4 were not statistically different among groups ($p > .050$). The bioluminescent signals in groups 2 to 4 were markedly lower than that of group 1, whereas the difference was statistically significant only between groups 1 and 4 ($p = .010$). The bioluminescent signal changes in groups 1 to 4 were significantly correlated with the tumor volume changes for 21 days ($p = .004$). No statistical difference was detected in bioluminescent signal change between groups 5 and 6, however (data not shown). Figure 4C shows significant correlation between K^{trans} changes for 3 days in the peripheral tumor regions of groups 1 to 4 (shown in Figure 2B) and tumor volume changes over 21 days (shown in Figure 4A) ($p < .001$). The K^{trans} changes for 2 days post–therapy initiation were also significantly correlated with the tumor volume changes over 21 days ($p = .001$), but those for 1 day were not ($p = .550$). Similarly, Figure 4D shows the positive correlation between K^{trans} changes for 3 days in the peripheral tumor regions of groups 1 to 4 and the normalized bioluminescent signal changes over 21 days (shown in Figure 4B), with statistical significance ($p = .050$).

Early K^{trans} change was significantly correlated with microvessel and proliferating cell densities. Figure 5A shows representative microphotographs of CD31 and Ki-67 staining of tumor tissues of groups 1 to 4 collected at day 21, with the microvessel areas and proliferating cells indicated with black arrows in each subfigure. Quantifications of microvessel (CD31 positive) and proliferating cell (Ki-67 positive) densities of groups 1 to 4 are presented in Figure 5B and C, respectively. The microvessel densities of groups 2 to 4 were significantly lower than that of group 1 ($p < .050$) (see Figure 5B), whereas the proliferating cell density only after combination therapy (group 4) was significantly lower than that of group 1 ($p < .001$) (see Figure 5C). The changes in K^{trans} values at 3 days in the peripheral tumor region of groups 1 to 4 were significantly and positively correlated with both the microvessel densities ($p = .002$) (see Figure 5D) and the proliferating cell densities ($p = .001$) (see Figure 5E).

A new, DCE-MRI-based biomarker to measure therapeutic efficacy independent of an imaging time point was proposed. Figure 6A shows the mean K^{trans} changes in groups 1 to 4 during 3 days of therapy in the peripheral tumor region (shown in Figure 2B), together with the best-fitting quadratic curves for the four groups. Assuming that the early K^{trans} changes in tumors owing to effective therapies follow quadratic curves, validated with high R^2 values in Figure 6A (≥ .73), the best-fitting quadratic curve for the K^{trans} change at 3 days for each tumor was retrieved. The quadratic coefficients of the curves for groups 1 to 4 are shown in

Figure 6B; those of groups 3 and 4 were significantly lower than that of the control ($p = .006$ and .003, respectively). The quadratic coefficients were significantly correlated with tumor volume changes over 21 days ($p < .001$), normalized bioluminescent signal changes over 21 days ($p = .019$), microvessel densities ($p = .002$), and proliferating cell densities ($p = .001$) (Figure 6, C–F).

Discussion

To our knowledge, we report the first DCE-MRI study using an orthotopic pancreatic tumor mouse model, evaluating early therapeutic efficacy of cetuximab and/or irinotecan. These findings support the potential for clinical use of DCE-MRI as an early prognostic tool assessing an effective pancreatic cancer treatment for an individual patient. One direct clinical benefit of this approach would be to identify patients resistant to standard therapy with gemcitabine and erlotinib early in the course of therapy and preclude unnecessary side effects. As other targeted agents are developed for pancreatic cancer, ultimately, the optimal treatment for each individual patient could be determined with a stepwise early therapeutic assessment approach using DCE-MRI. An additional noninvasive MRI modality such as diffusion-weighted imaging (DWI) may further enhance the accuracy of the predictive or prognostic decision. DWI is able to detect the amplitude of water mobility owing to thermodynamic effect, and apparent diffusion coefficient (ADC) is proportional to the amplitude of water diffusion. During apoptosis or necrosis induced by effective therapy, water in the extracellular space is increased, and the change in ADC can be measured based on DWI. A significant ADC increase in orthotopic pancreatic tumors was detected at only 1 day after anti-DR5 therapy, prior to visible change in tumor morphology or size, in our previous study.[21] The clinical practicality of DCE-MRI for the typically hypovascular pancreatic adenocarcinoma has been questioned owing to resultant lower signal to noise ratio (SNR) in quantitative analysis.[34] However, the high-field strength magnetic resonance approach may diminish this concern because the SNR is linearly proportional to the magnetic field strength; we presented the feasibility of quantitative DCE-MRI for human pancreatic adenocarcinoma using a 3 T magnetic resonance scanner (Achieva Quasar 3T, Philips Healthcare, Best, Netherlands).[35]

A relatively novel quantification approach known as the RR model was employed to calculate K^{trans} and ν_e values in this study.[25,27,36] In the Tofts model, the concentration of a contrast agent in blood plasma, named AIF, needs to be measured to quantify the contrast agent transfer in tissue microvasculature.[26] However, the accurate measurement of AIF requires high temporal resolution (less than 10 seconds usually), compromised with spatial resolution and SNR. Instead, in the RR model, the signal enhancement in an RR (usually muscle tissue) is measured to obviate the need for AIF measurement. The major concern of this method may be the fact that the fractional extravascular-extracellular volume in the RR ($\nu_{e,RR}$) should be assumed; when the perivertebral muscle tissue was designated as the RR, the measured $\nu_{e,RR}$ was 0.0797 ± 0.0276 (mean ± SD) in nine rats.[27] However, assuming that fractional extravascular-extracellular volume in the same RR of each mouse does not vary significantly for a short period of time, the RR model can be considered a reasonable alternative when the reliable AIF is not available.

Lower K^{trans} and ν_e values were observed in the central tumor area. It follows that the SNR in the central tumor region should also be lower. Thus, confining ROI to only the peripheral tumor region is a reasonable approach to improve measurement accuracy. In our study, this phenomenon may explain the markedly decreased variability (standard error) of the K^{trans} and ν_e values relative to those at day 0 using the peripheral region analysis. Peripheral tumor region analysis has been employed during DCE-MRI by many investigators,[37,38] but segmentation was implemented manually in most cases. In contrast, our method determined

the inner boundary of the region automatically, maintaining the random topology of the outer boundary and a constant thickness around the rim; this might also produce improved accuracy of this segmentation method. The region of viable tumor tissue can be identified via multispectral analysis, but additional diffusion and transverse relaxation rate (R_2) maps would be required.[39]

The nonlinear response of intratumoral K^{trans} change during the early therapy stage was determined by repeated DCE-MRI, and an indicator to characterize the nonlinearity was proposed as a new biomarker. This indicator might facilitate evaluation of the therapeutic efficacy of drugs independent of an imaging time point. However, given that the pancreatic adenocarcinoma is typically hypovascular, our findings would be more convincing if a tumorgraft model was used (xenograft directly implanted from a patient without cell culturing).[40] However, the tumorgrafts from primary specimens have a high percentage of growth failure; therefore, it may not be practical owing to high expense in time and resources. Therefore, our orthotopic pancreatic tumor xenograft model is an alternative and perhaps more practical approach to study the physiologic changes of pancreatic cancer. In addition, higher signal enhancements were observed at the peripheral region of human pancreatic adenocarcinoma during DCE-MRI using a 3 T clinical magnetic resonance system (Dr. Desiree Morgan, UAB, personal communication, 2010), which shows the possibility that the boundary of some pancreatic tumors could be highly vascular, even if a large portion of the tumor region was not. Therefore, our model may provide useful information to predict human tumor response at the peripheral region, but more investigations are needed. Although gadolinium-based magnetic resonance contrast agents are generally considered safe at the recommended dosage for patients without chronic renal failure,[41] sequential DCE-MR examinations over a short period of time would be additionally stressful for patients undergoing chemotherapy and cost inefficient. Therefore, it would be better to determine the optimal imaging time point after therapy initiation, maximizing the accuracy of therapy evaluation, after standardizing the nonlinear tumor response via the additional preclinical and clinical magnetic resonance experiments.

Acknowledgments

We thank Sharon Samuel for assistance with tumor cell implantation, SPECT/CT imaging, and biodistribution study and Drs. Erik D. Dohm and James A. Posey for valuable consultations. All experiments complied with current regulatory requirements (including ethics requirements) and the laws of the United States of America.

Financial disclosure of authors: Grant support was as follows: American Association for Cancer Research-Pancreatic Cancer Action Network (AACR-PANCAN) Career Development Award, UAB Translational Research Grant, HSF-GEF Scholar Award, and National Institutes of Health grants 5P50CA89019, P20CA10195, and 5P30CA013148.

References

1. Presentation from the American Cancer Society. Cancer Statistics. 2009 Available at: http://www.cancer.org/docroot/PRO/content/PRO_1_1_Cancer_Statistics_2009_presentation.asp.
2. Wray CJ, Ahmad SA, Matthews JB, et al. Surgery for pancreatic cancer: recent controversies and current practice. Gastroenterology. 2005; 128:1626–1641. [PubMed: 15887155]
3. Burris HA III, Moore MJ, Andersen J, et al. Improvements in survival and clinical benefit with gemcitabine as first-line therapy for patients with advanced pancreas cancer: a randomized trial. J Clin Oncol. 1997; 15:2403–2413. [PubMed: 9196156]
4. Loehrer PJ, Powell ME, Cardenes HR, et al. A randomized phase III study of gemcitabine in combination with radiation therapy versus gemcitabine alone in patients with localized, unresectable pancreatic cancer: E4201. J Clin Oncol. 2008; 26(Suppl):4506.
5. Berlin JD, Catalano P, Thomas JP, et al. Phase III study of gemcitabine in combination with fluorouracil versus gemcitabine alone in patients with advanced pancreatic carcinoma: Eastern

Cooperative Oncology Group Trial E2297. J Clin Oncol. 2002; 20:3270–3275. [PubMed: 12149301]

6. Heinemann V, Quietzsch D, Gieseler F, et al. Randomized phase III trial of gemcitabine plus cisplatin compared with gemcitabine alone in advanced pancreatic cancer. J Clin Oncol. 2006; 24:3946–3952. [PubMed: 16921047]
7. Rocha Lima CM, Green MR, Rotche R, et al. Irinotecan plus gemcitabine results in no survival advantage compared with gemcitabine monotherapy in patients with locally advanced or metastatic pancreatic cancer despite increased tumor response rate. J Clin Oncol. 2004; 22:3776–3783. [PubMed: 15365074]
8. Louvet C, Labianca R, Hammel P, et al. Gemcitabine in combination with oxaliplatin compared with gemcitabine alone in locally advanced or metastatic pancreatic cancer: results of a GERCOR and GISCAD phase III trial. J Clin Oncol. 2005; 23:3509–3516. [PubMed: 15908661]
9. Tobita K, Kijima H, Dowaki S, et al. Epidermal growth factor receptor expression in human pancreatic cancer: significance for liver metastasis. Int J Mol Med. 2003; 11:305–309. [PubMed: 12579331]
10. Xiong HQ, Rosenberg A, LoBuglio A, et al. Cetuximab, a monoclonal antibody targeting the epidermal growth factor receptor, in combination with gemcitabine for advanced pancreatic cancer: a multicenter phase II trial. J Clin Oncol. 2004; 22:2610–2616. [PubMed: 15226328]
11. Rubin Grandis J, Melhem MF, Gooding WE, et al. Levels of TGF-alpha and EGFR protein in head and neck squamous cell carcinoma and patient survival. J Natl Cancer Inst. 1998; 90:824–832. [PubMed: 9625170]
12. Moore MJ, Goldstein D, Hamm J, et al. Erlotinib plus gemcitabine compared with gemcitabine alone in patients with advanced pancreatic cancer: a phase III trial of the National Cancer Institute of Canada Clinical Trials Group. J Clin Oncol. 2007; 25:1960–1966. [PubMed: 17452677]
13. Chhieng DC, Jhala D, Jhala N, et al. Endoscopic ultrasound-guided fine-needle aspiration biopsy: a study of 103 cases. Cancer. 2002; 96:232–239. [PubMed: 12209665]
14. Evelhoch JL, Gillies RJ, Karczmar GS, et al. Applications of magnetic resonance in model systems: cancer therapeutics. Neoplasia. 2000; 2:152–165. [PubMed: 10933074]
15. Desjardins A, Barboriak DP, Herndon JE, et al. Dynamic contrast-enhanced magnetic resonance imaging (DCE-MRI) evaluation in glioblastoma (GBM) patients treated with bevacizumab (BEV) and irinotecan (CPT-11). J Clin Oncol. 2007; 25(Suppl):2029.
16. Cheung YC, Chen SC, Su MY, et al. Monitoring the size and response of locally advanced breast cancers to neoadjuvant chemotherapy (weekly paclitaxel and epirubicin) with serial enhanced MRI. Breast Cancer Res Treat. 2003; 78:51–58. [PubMed: 12611457]
17. Martincich L, Montemurro F, De Rosa G, et al. Monitoring response to primary chemotherapy in breast cancer using dynamic contrast-enhanced magnetic resonance imaging. Breast Cancer Res Treat. 2004; 83:67–76. [PubMed: 14997056]
18. Baba Y, Furusawa M, Murakami R, et al. Role of dynamic MRI in the evaluation of head and neck cancers treated with radiation therapy. Int J Radiat Oncol Biol Phys. 1997; 37:783–787. [PubMed: 9128952]
19. Morgan B, Thomas AL, Drevs J, et al. Dynamic contrast-enhanced magnetic resonance imaging as a biomarker for the pharmacological response of PTK787/ZK 222584, an inhibitor of the vascular endothelial growth factor receptor tyrosine kinases, in patients with advanced colorectal cancer and liver metastases: results from two phase I studies. J Clin Oncol. 2003; 21:3955–3964. [PubMed: 14517187]
20. Rosen MA, Schnall MD. Dynamic contrast-enhanced magnetic resonance imaging for assessing tumor vascularity and vascular effects of targeted therapies in renal cell carcinoma. Clin Cancer Res. 2007; 13:770s–776s. [PubMed: 17255308]
21. Kim H, Morgan DE, Buchsbaum DJ, et al. Early therapy evaluation of combined anti-death receptor 5 antibody and gemcitabine in orthotopic pancreatic tumor xenografts by diffusion-weighted magnetic resonance imaging. Cancer Res. 2008; 68:8369–8376. [PubMed: 18922909]
22. Abrams MJ, Juweid M, tenKate CI, et al. Technetium-99m-human polyclonal IgG radiolabeled via the hydrazino nicotinamide derivative for imaging focal sites of infection in rats. J Nucl Med. 1990; 31:2022–2028. [PubMed: 2266401]

23. Larsen SK, Solomon HF, Caldwell G, et al. [99mTc]tricine: a useful precursor complex for the radiolabeling of hydrazinonicotinate protein conjugates. Bioconjug Chem. 1995; 6:635–638. [PubMed: 8974465]
24. Lowry O, Rosebrough N, Farr L, et al. Protein measurement with the folin phenol reagent. J Biol Chem. 1951; 193:265–275. [PubMed: 14907713]
25. Yankeelov TE, Luci JJ, Lepage M, et al. Quantitative pharmacokinetic analysis of DCE-MRI data without an arterial input function: a reference region model. Magn Reson Imaging. 2005; 23:519–529. [PubMed: 15919597]
26. Tofts PS, Brix G, Buckley DL, et al. Estimating kinetic parameters from dynamic contrast-enhanced T(1)-weighted MRI of a diffusable tracer: standardized quantities and symbols. J Magn Reson Imaging. 1999; 10:223–232. [PubMed: 10508281]
27. Yankeelov TE, Cron GO, Addison CL, et al. Comparison of a reference region model with direct measurement of an AIF in the analysis of DCE-MRI data. Magn Reson Med. 2007; 57:353–361. [PubMed: 17260371]
28. Pezold JC, Zinn K, Talbert MA, et al. Validation of ultrasonography to evaluate murine orthotopic oral cavity tumors. ORL J Otorhinolaryngol Relat Spec. 2006; 68:159–163. [PubMed: 16465070]
29. Sternberg SR. Biomedical image processing. IEEE Computer. 1983; 16:22–34.
30. Hertzog C, Rovine M. Repeated-measures analysis of variance in developmental research: selected issues. Child Dev. 1985; 56:787–809. [PubMed: 4042744]
31. Neter, J.; Kutner, MH.; Nachtsheim, JC., et al. Applied linear statistical models. 4th ed.. Columbus, OH: The McGraw-Hill Companies; 1996.
32. Sokal, RR.; Rohlf, FJ. Biometry: the principles and practice of statistics in biological research. New York: W.H. Freeman; 1995.
33. Rodgers JL, Nicewander WA. Thirteen ways to look at the correlation coefficient. American Statistician. 1988; 42:59–66.
34. Hosoki T. Dynamic CT of pancreatic tumors. AJR Am J Roentgenol. 1983; 140:959–965. [PubMed: 6601441]
35. Morgan DE, Kim H, Ng T, et al. Quantitative perfusion and diffusion-weighted MR imaging of pancreatic adenocarcinoma at 3T: a pilot study. AJR Am J Roentgenol. 2009; 192:A49–A52.
36. Yankeelov TE, DeBusk LM, Billheimer DD, et al. Repeatability of a reference region model for analysis of murine DCE-MRI data at 7T. J Magn Reson Imaging. 2006; 24:1140–1147. [PubMed: 17024660]
37. Kiessling F, Farhan N, Lichy MP, et al. Dynamic contrast-enhanced magnetic resonance imaging rapidly indicates vessel regression in human squamous cell carcinomas grown in nude mice caused by VEGF receptor 2 blockade with DC101. Neoplasia. 2004; 6:213–223. [PubMed: 15153333]
38. Niermann KJ, Fleischer AC, Huamani J, et al. Measuring tumor perfusion in control and treated murine tumors: correlation of microbubble contrast-enhanced sonography to dynamic contrast-enhanced magnetic resonance imaging and fluorodeoxyglucose positron emission tomography. J Ultrasound Med. 2007; 26:749–756. [PubMed: 17526606]
39. Carano RA, Ross AL, Ross J, et al. Quantification of tumor tissue populations by multispectral analysis. Magn Reson Med. 2004; 51:542–551. [PubMed: 15004796]
40. Fiebig HH, Maier A, Burger AM. Clonogenic assay with established human tumour xenografts: correlation of in vitro to in vivo activity as a basis for anticancer drug discovery. Eur J Cancer. 2004; 40:802–820. [PubMed: 15120036]
41. Grobner T, Prischl FC. Gadolinium and nephrogenic systemic fibrosis. Kidney Int. 2007; 72:260–264. [PubMed: 17507905]

Appendix

APPENDIX A: Mouse Port Implantation and Maintenance

Each mouse was anesthetized with an intraperitoneal injection of sodium pentobarbital (60–65 mg/kg body weight [BW], Nembutal sodium solution, Abbott Laboratories, North Chicago, IL) in 0.2 mL of saline and placed in supine position on the operative field. A 0.7–

1.0 -cm incision in an area of the mouse back was made for implanting the mouse port. A subcutaneous pocket was made by insertion of hemostats (micro-mosquito hemostat, Fine Science Tools Inc., Foster City, CA), and then the port was implanted into the pocket. Another skin incision (0.5 cm) was made in the neck area to expose a jugular vein, and a canal was created under the skin between two incisions using a straight forceps. The catheter connected to the port was held and dragged through the canal, and was introduced into the jugular vein. The vein was isolated and secured with two 7-0 sutures. After surgery, each mouse was injected intramuscularly with 2 mg/kg BW of buprenorphine hydrochloride (Buprenex, Hospira Inc., Lake Forest, IL) in 0.2 mL of saline for analgesia. The cage containing the mice was then placed on a SoftHeat Heating Pad (Kaz Inc., Southborough, MA) for about 1 hour during recovery from surgery. The port was rinsed with heparin (8.6 U/mL) in 0.1 mL of phosphate-buffered saline (PBS, pH: 7.4) every 24 hours, to prevent blood coagulation inside of the catheter. The lumen of the port had 0.05 mL dead volume, so the heparin solution was mixed with gadoteridol (0.0267 mmol/mL) to fill the dead volume with gadoteridol and avoid dilution.

APPENDIX B: Tumor Tissue Staining

Each tumor was sliced into two pieces, and then immersed into 10% neutral buffered formalin overnight at room temperature. Tissue sections of 5 μm thickness were cut on an Accu-Cut SRM microtome (Sakura, Tokyo, Japan). Sections of paraffin embedded tissue were mounted on Bond-Rite slides from Richard-Allan Scientific (Kalamazoo, MI) and heated at 60°C for 2 hours. Paraffin was removed from the sections by three changes of xylene and rehydrated through graded alcohols from absolute to 70% for 5 minutes each.

Antigen retrieval for the CD31 antibody was performed with high temperature treatment with pH 10 Tris buffer 0.5 M. H_2O_2 avidin and biotin solutions and 3% goat serum were used to quench peroxidases, block endogenous biotin and block nonspecific binding. Rabbit polyclonal antibody to CD31 (Abcam Inc., Cambridge, MA) was diluted 1:200 and applied to the tissue at room temperature for 1 hour. The secondary antibody was goat anti-rabbit (Jackson Immuno Research, West Grove, PA) and the label was avidin-HRP (Signet Pathology Systems, Dedham, MA). After the DAB chromagen (BioGenex, San Ramon, CA) was applied, the tissues were counterstained with hematoxylin and the cover slips mounted with Permount. Antigen retrieval for Ki67 was performed at high temperature in pH 9 Tris ethylenediaminetetraacetic acid. Rabbit monoclonal antibody to Ki67 (Neomarkers, Freemont, CA) was diluted 1:750 and applied for 1 hour at room temperature. Quenching, blocking and localization of Ki67 were the same as for CD31.

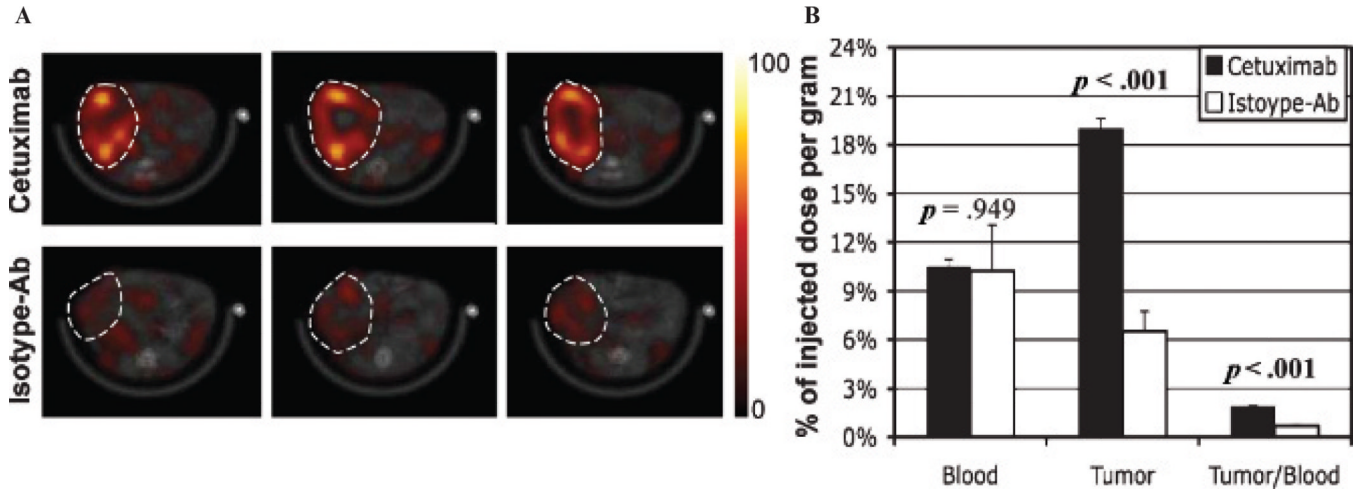

Figure 1.

A, In vivo SPECT/CT fused images (transaxial view) showing distribution of ^{99m}Tc-cetuximab (*upper row*) or ^{99m}Tc-isotype control antibody (*lower row*) of two representative SCID mice bearing orthotopic pancreatic tumors at ~6 hours postinjection. The three images in each row were obtained from the same mouse, and the spacing between the neighboring images is 1.55 mm. The tumor boundary is indicated with a *white dotted circle* in each subfigure; the same color scale was applied for all SPECT images. *B*, Biodistributions of ^{99m}Tc-cetuximab (mean and SE) and ^{99m}Tc-isotype control antibody in blood, tumor, and tumor to blood ratio at 24 hours after intravenous dose injection. The *p* values above bars represent the statistical difference between the two groups.

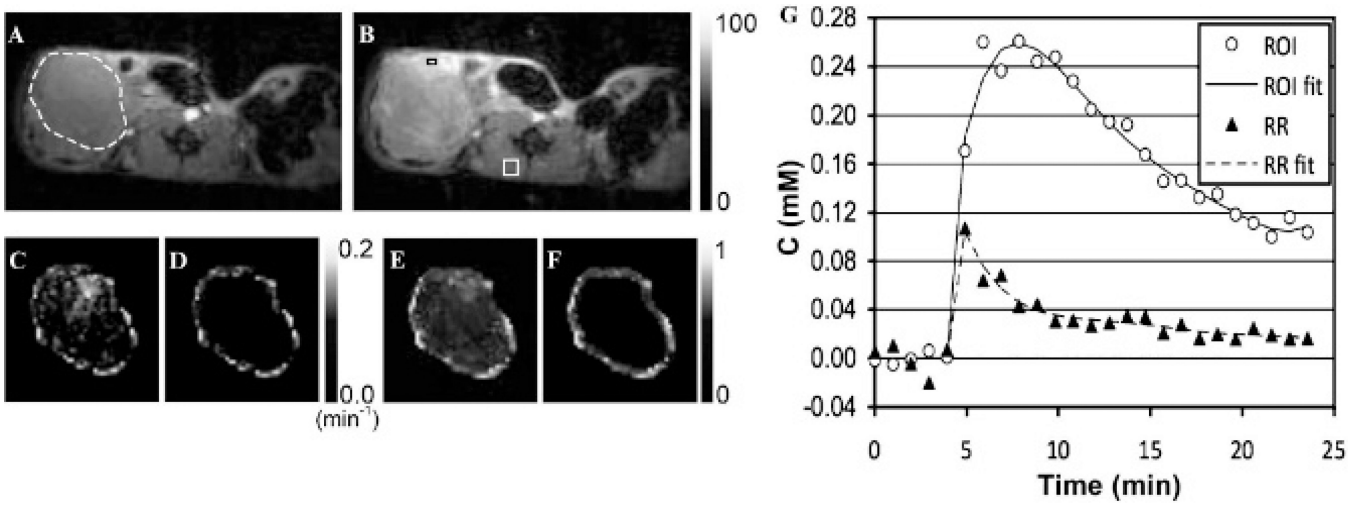

Figure 2.

Representative dynamic contrast-enhanced magnetic resonance images of a SCID mouse bearing an orthotopic pancreatic tumor at (A) 1 minute before and (B) 2 minutes after gadoteridol injection u sing the same intensity scale (from 0 to 100) when maximum value is normalized to 100, with (C, D) K^{trans} and (E, F) v_e maps of the (C, E) entire tumor regions or (D, F) 0.5 mm–thick peripheral tumor regions. *G*, Contrast enhancement curves averaged in the region of interest (ROI) and reference region (RR) indicated with the *black rectangle* (2 × 1 window: 2 pixels) and the *white square* (4 × 4 window: 16 pixels), respectively, in the subfigure (B), together with the best-fitting fifth-order polynomial curves. The boundary of the tumor region is indicated with a *white dotted circle* in A.

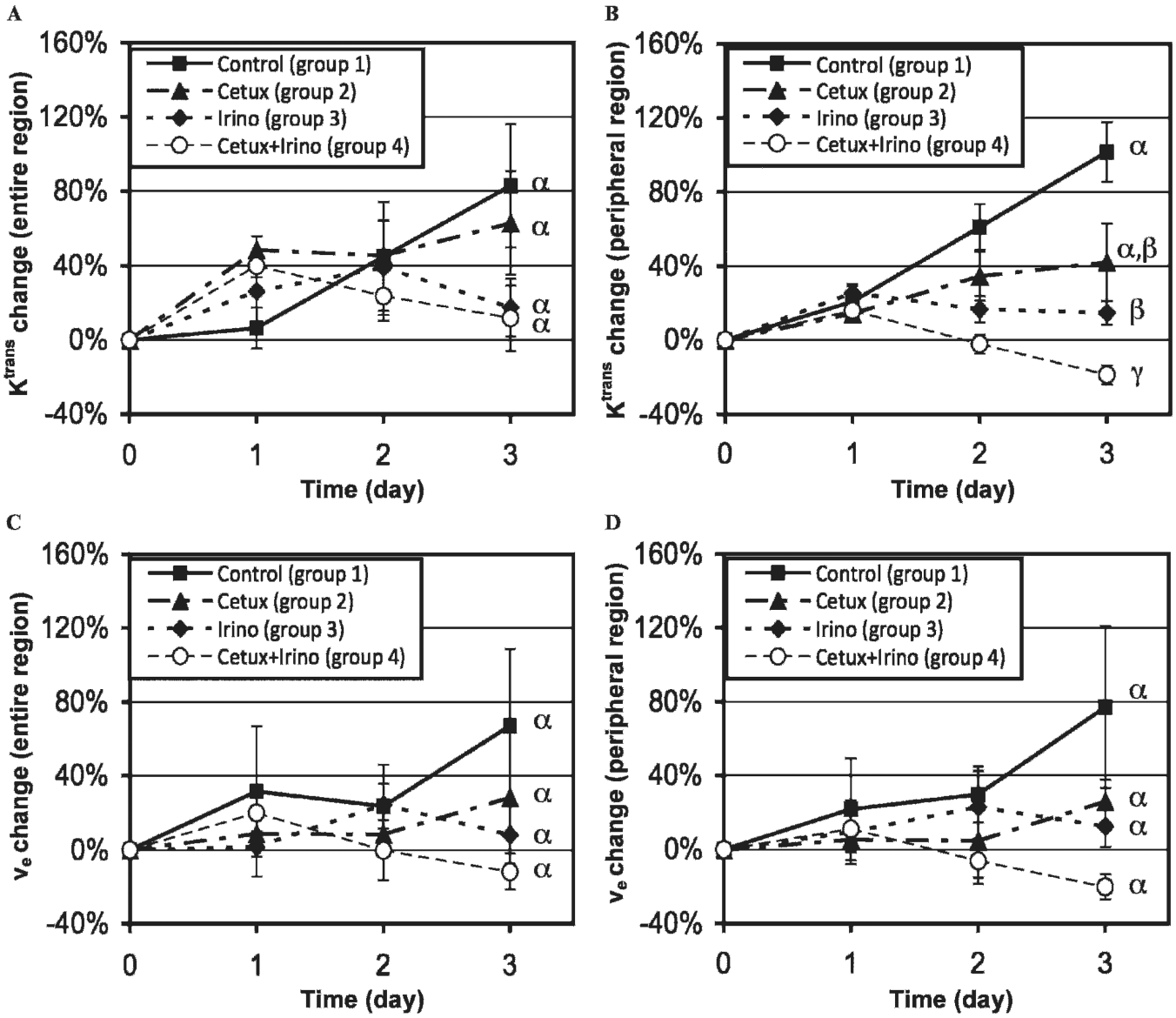

Figure 3.

K^{trans} changes (A, B) or v_e changes (C, D) of groups 1 to 4 during 3 days posttherapy in the entire tumor region (A, C) or peripheral tumor region (B, D). Different Greek letters represent statistical differences among the groups during 3 days.

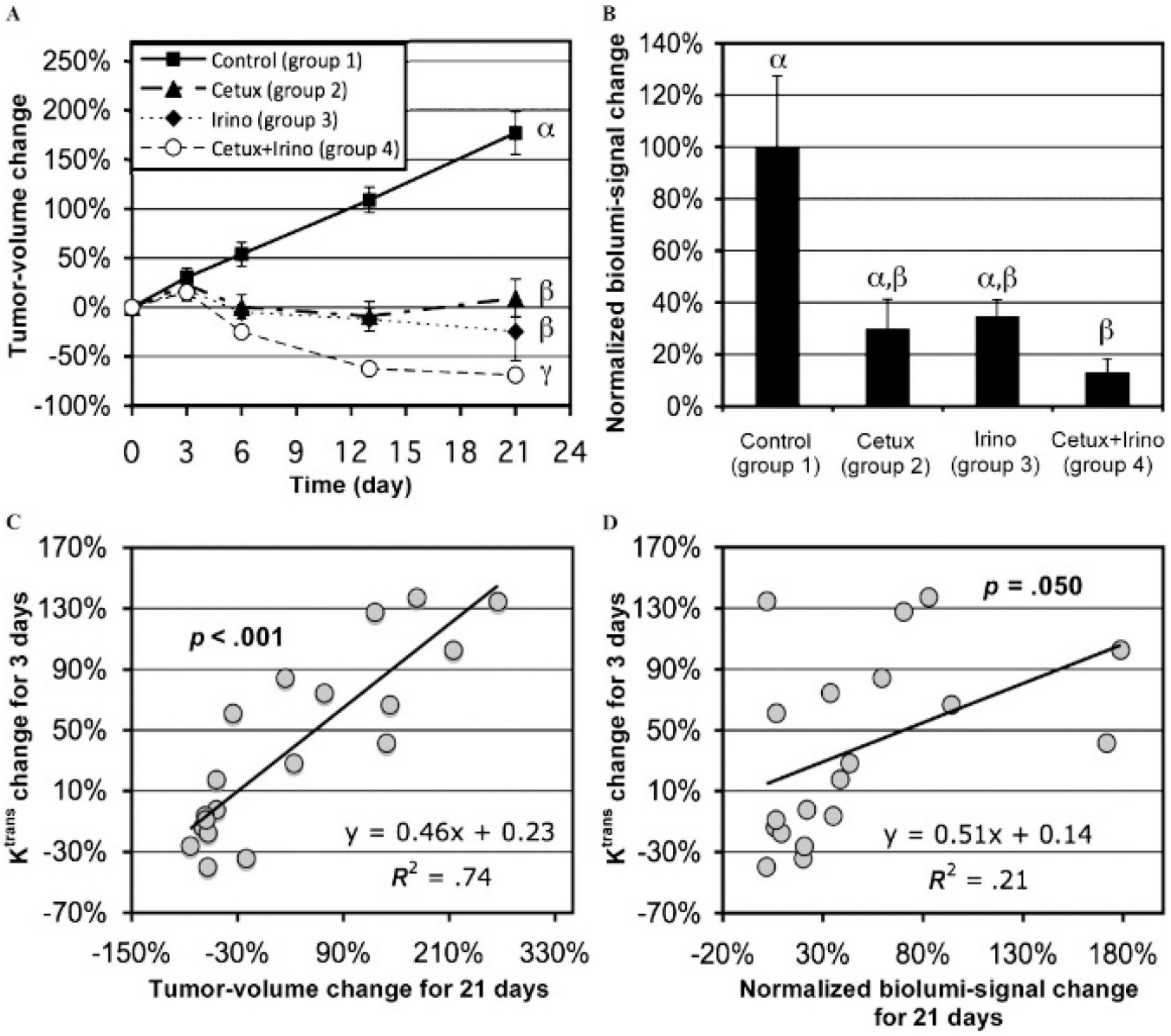

Figure 4.

Tumor volume changes (A) or normalized bioluminescent signal changes (B) of groups 1 to 4 during 21 days after therapy initiation; different Greek letters present statistical differences among the groups. K^{trans} changes in the peripheral tumor region of groups 1 to 4 during 3 days after therapy initiation versus tumor volume changes (C) or normalized bioluminescent signal changes (D) for 21 days after therapy initiation; *p* values represent the significance of the correlation.

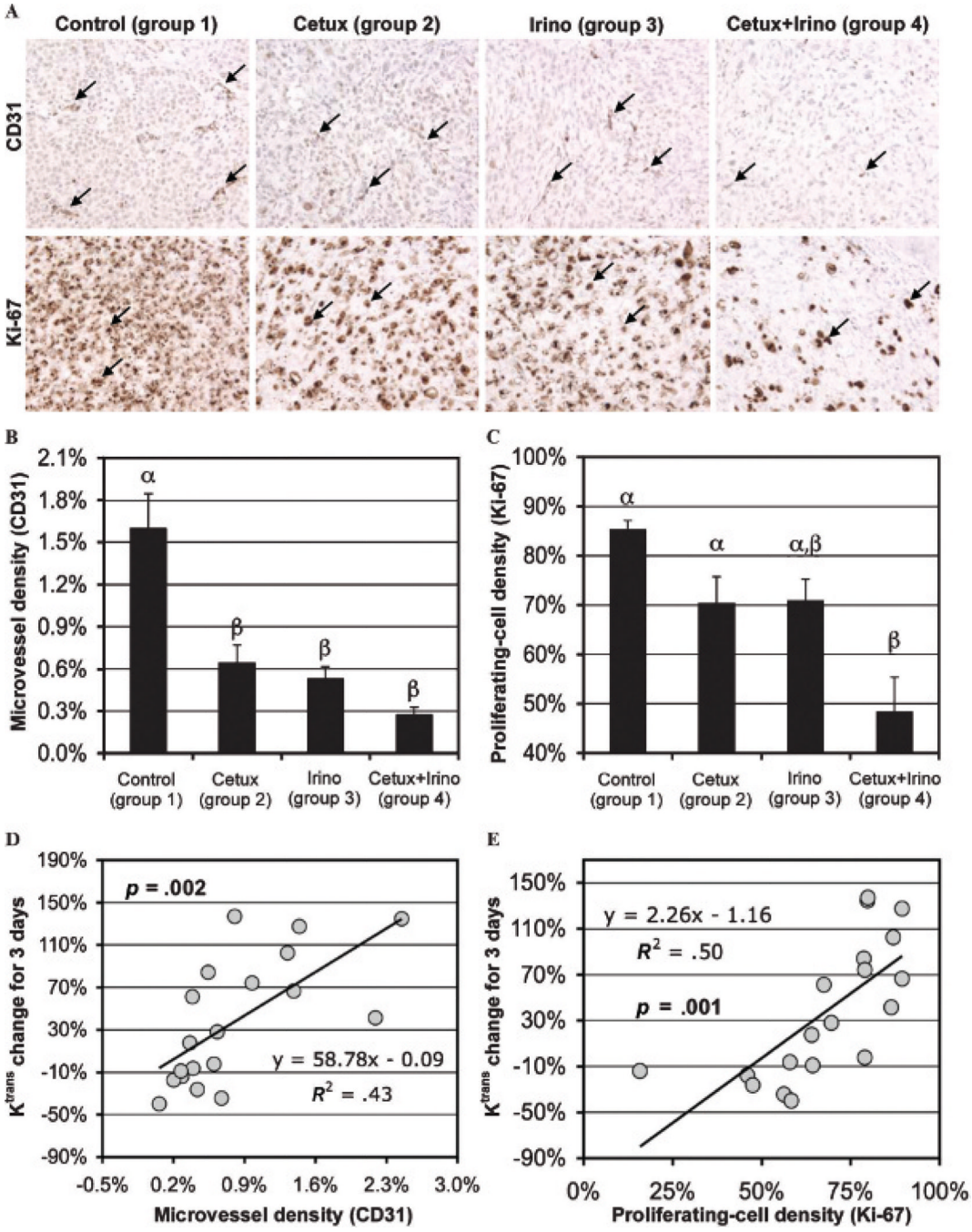

Figure 5.

A, Representative microphotographs of CD31 (×400 original magnification) and Ki-67 (×400 original magnification) staining of MIA PaCa-2 tumors of groups 1 to 4 collected at day 21; the microvessel areas and proliferating cells are indicated with *black arrows* in each row. Microvessel (B, CD31 expressed) and proliferating (C, Ki-67 expressed) cell densities of groups 1 to 4 are presented; statistical differences among groups are indicated by different Greek letters above bars. K^{trans} changes in the peripheral tumor region of groups 1 to 4 during 3 days after therapy initiation versus (D) microvessel and (E) proliferating cell densities; *p* values represent the significance of the correlation.

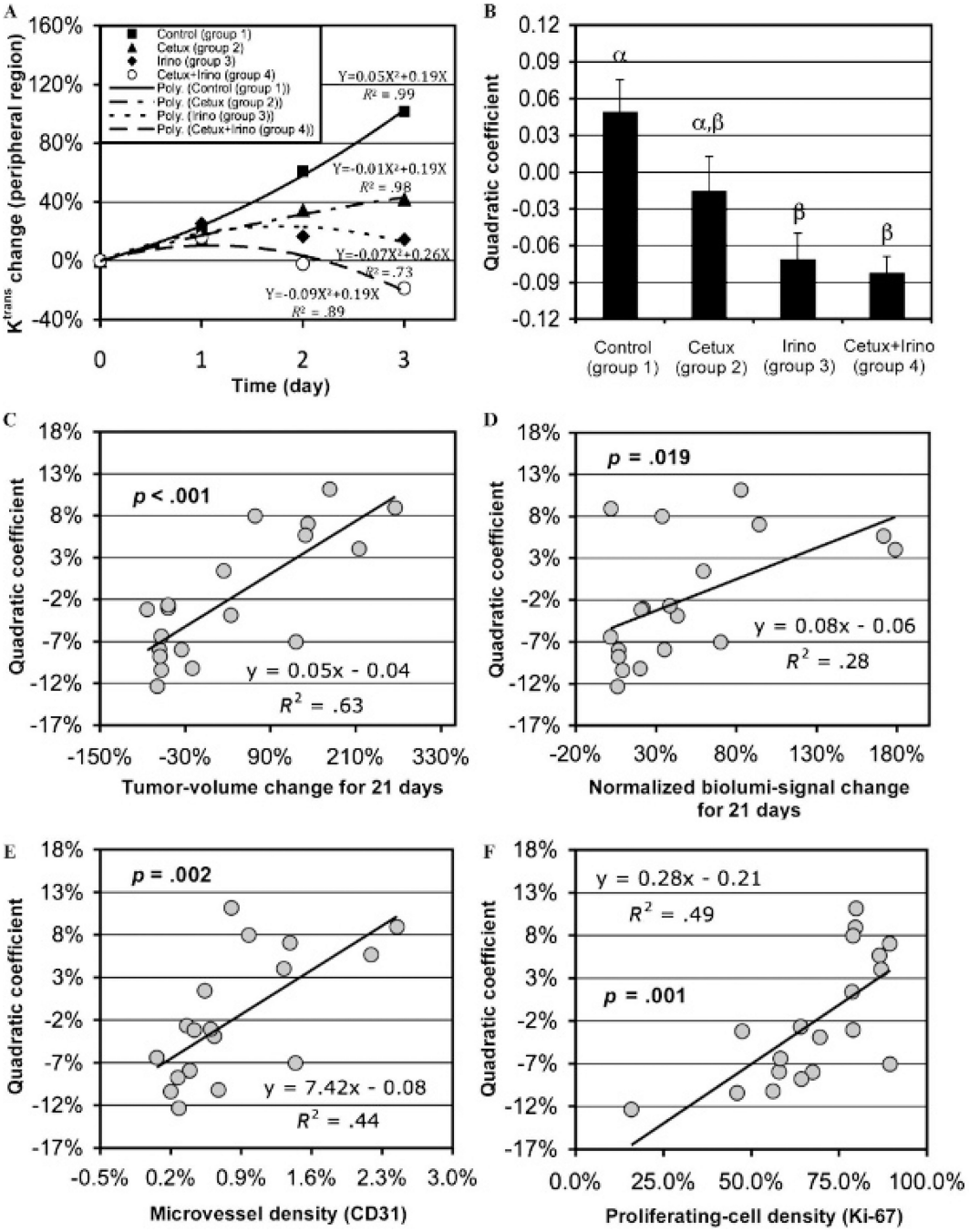

Figure 6.

A, Mean K^{trans} changes of groups 1 to 4 during 3 days post–therapy initiation in the peripheral tumor region with the best-fitting second-order polynomial curves for the four groups. *B*, Quadratic coefficients of the best-fitting second-order polynomial curves to the K^{trans} changes in the peripheral tumor region of groups 1 to 4 (mean and SE); different Greek letters represent statistical differences among the groups. The quadratic coefficients shown in B versus (C) tumor volume changes for 21 days, (D) normalized bioluminescent signal changes for 21 days, (E) microvessel densities, and (F) proliferating cell densities; *p* values represent the significance of the correlation.

Table 1

Study Protocol Showing the Schedules of Dosing and Imaging of Groups 1 to 8

	Hours, Days											
Mouse	**0 h**	**6 h**	**24 h**	**2 d**	**3 d**	**6 d**	**7 d**	**10 d**	**13 d**	**14 d**	**17 d**	**21 d**
Group 1 (PBS)	Bio Dce Ana Inj (*n* = 6)		Dce Ana (*n* = 6)	Dce Ana (*n* = 6)	Dce Ana Inj (*n* = 6)	Ana (*n* = 6)	Inj (*n* = 6)	Inj (*n* = 6)	Ana (*n* = 6)	Inj (*n* = 6)	Inj (*n* = 6)	Bio (*n* = 6)
Group 2 (cetuximab)	Bio Dce Ana Inj (*n* = 6)		Dce Ana (*n* = 6)	Dce Ana (*n* = 6)	Dce Ana Inj (*n* = 6)	Ana (*n* = 6)	Inj (*n* = 6)	Inj (*n* = 5)	Ana (*n* = 5)	Inj (*n* = 5)	Inj (*n* = 5)	Bio (*n* = 4)
Group 3 (irinotecan)	Bio Dce Ana Inj (*n* = 6)		Dce Ana (*n* = 6)	Dce Ana (*n* = 6)	Dce Ana Inj (*n* = 6)	Ana (*n* = 6)	Inj (*n* = 5)	Inj (*n* = 4)	Ana (*n* = 3)	Inj (*n* = 3)	Inj (*n* = 3)	Bio (*n* = 3)
Group 4 (cetuximab + irinotecan)	Bio Dce Ana Inj (*n* = 6)		Dce Ana (*n* = 6)	Dce Ana (*n* = 6)	Dce Ana Inj (*n* = 6)	Ana (*n* = 6)	Inj (*n* = 6)	Inj (*n* = 6)	Ana (*n* = 6)	Inj (*n* = 6)	Inj (*n* = 6)	Bio (*n* = 6)
Group 5 (PBS)	Bio Dce Ana Inj (*n* = 3)			Bio Dce Ana Inj (*n* = 3)	Bio Ana (*n* = 3)							
Group 6 (cetuximab + irinotecan)	Bio Dce Ana Inj (*n* = 4)			Bio Dce Ana Inj (*n* = 4)	Bio Ana (*n* = 4)							
Group 7 (^{99m}Tc control antibody)	Inj (*n* = 4)	SPECT, CT (*n* = 4)	BioD (*n* = 4)									
Group 8 (^{99m}Tc-cetuximab)	Inj (*n* = 5)	SPECT, CT (*n* = 5)	BioD (*n* = 5)									

Ana = anatomic magnetic resonance imaging; Bio = bioluminescence imaging; BioD = biodistribution study; CT = computed tomography; Dce = dynamic contrast-enhanced magnetic resonance imaging; Inj = dose injection; PBS = phosphate-buffered saline; SPECT = single-photon emission computed tomography.

The number of animals is given at each time point. The dose used for each group is shown with group number.